Vol. 91 No. 6 pp. 2041–2057 ACTA GEOLOGICA SINICA (English Edition) Dec. 2017

Archean-Paleoproterozoic Lithospheric Mantle at the Northern Margin of the North China Craton Represented by Tectonically Exhumed Peridotites

TIAN Wei[1, *], WANG Shuangyue[1], LIU Fenglin[1], CHU Zhuyin[2], WANG Bin[1], CHEN Mimi[2,3] and Jennifer PRICHARD[3]

1 *Key Laboratory of Orogenic Belts and Crustal Evolution, MOE, School of Earth and Space Sciences, Peking University, Beijing 100871, China*

2 *State Key Laboratory of Lithospheric Evolution, Institute of Geology and Geophysics, Chinese Academy of Sciences, Beijing 100029, China*

3 *Research School of Earth and Space Sciences, the Australian National University, ACT 0200, Australia*

Abstract: Tectonically emplaced peridotites from North Hebei Province, North China Craton, have retained an original harzburgite mineral assemblage of olivine (54%–58%) + orthopyroxene (40%–46%) +minor clinopyroxene (<1%)+spinel. Samples with boninite-like chemical compositions also coexist with these peridotites. The spinels within the peridotites have high-Al end-members with Al_2O_3 content of 30 wt%–50 wt%, typical of mantle spinels. When compared with experimentally determined melt extraction trajectories, the harzburgites display a high degree of melting and enrichment of SiO_2, which is typical of cratonic mantle peridotites. The peridotites display variably enriched light rare earth elements (REEs), relatively depleted middle REEs and weakly fractionated heavy REEs, which suggest a melt extraction of over 25% in the spinel stability field. The occurrence of arc- and SSZ-type chromian spinels in the peridotites suggests that melt extraction and metasomatism occurred mostly in a subduction-related setting. This is also supported by the geochemical data of the coexisting boninite-like samples. The peridotites have $^{187}Os/^{188}Os$ ratios ranging from 0.113–0.122, which is typical of cratonic lithospheric mantle. These $^{187}Os/^{188}Os$ ratios yield model melt extraction ages (T_{RD}) ranging from 981 Ma to 2054 Ma, which may represent the minimum estimation of the melt extraction age. The Al_2O_3-$^{187}Os/^{188}Os$-proxy isochron ages of 2.4 Ga–2.7 Ga suggest a mantle melt depletion age between the Late Achaean and Early Paleoproterozoic. Both the peridotites and boninite-like rocks are therefore interpreted as tectonically exhumed continental lithospheric mantle of the North China Craton, which has experienced mantle melt depletion and subduction-related mantle metasomatism during the Neoarchean- Paleoproterozoic.

Key words: harzburgite, boninite, Re-Os isotopes, lithospheric mantle, Paleoproterozoic, North China Craton

1 Introduction

The North China Craton (NCC) is an Archean craton with a complicated geological evolution. Crustal rocks within the NCC record nearly all major global geological events in the early geotectonic history of the Earth (Zhai, 2011; Kusky et al., 2007; Wan et al., 2016; Zhao et al., 2016). In addition, a large set of petrological, geochemical, and Re-Os isotopic data of mantle-derived peridotite and pyroxenite xenoliths suggest a complex history for the lithospheric mantle below the NCC, particularly during the Archaen and Phanerozoic (e.g. Zheng et al., 1999; Gao et al., 2002; Li and Wang, 2002; Chu et al., 2009; Wu et al., 2006; Zhang et al., 2008; Tang et al., 2013). Due to their small size and limited occurrence however, these mantle xenoliths are incapable of providing the full picture surrounding the extent, all the timing of mantle melt depletion and past metasomatic processes of the NCC. In this study, we report for the first time, the discovery of a series of tectonically emplaced Archean to Paleoproterozoic mantle peridotites as well as

* Corresponding author. E-mail: davidtian@pku.edu.cn

© 2017 Geological Society of China

metamorphosed boninite-like rocks in the north margin of the NCC. We report a series of new data, including: (1) electron microprobe chemical analyses of minerals (olivine, orthopyroxene and spinel) that survived metasomatic alteration; (2) whole rock major element data and trace element data; and (3) whole rock Re-Os data. Using these data, we have characterized the early accretion history of the lithospheric mantle at the north margin of the NCC. Our findings also provide new temporal constraints for the initiation of subduction below the NCC.

2 Geological Background and Sampling

The northern margin of the NCC (Fig. 1) is bounded by the Xianghuangqi–Duolun–Chifeng fault belt to the north and by the Jining–Shangyi–Chicheng–Pingquan fault belt to the south (Hu et al., 2003). The key Precambrian geological units in this area include: (1) a series of Neoarchean tonalite-trondhjemite-granodiorite (TTG) gneisses and low grade metamorphosed volcanic-sedimentary rocks, which record the cratonization of the NCC (Zhai et al., 2011; Zhao et al., 2005; Peng et al., 2012); (2) Paleoproterozoic high pressure granulites and retrograde eclogites: the result of Proterozoic orogenic events in the NCC (Zhai et al., 1992; Zhai et al., 1995; Guo et al., 2001); and (3) a Paleoproterozoic khondalite belt (Wan et al., 2009; Liu et al., 2016) containing local ultra-high temperature metamorphic rocks (Guo et al., 2006) and basic intrusive rocks indicative of excess mantle potential temperatures (Peng et al, 2010). These samples together suggest a reworking process likely accompanied by a mantle plume event (Zhai et al., 2011).

A mafic-ultramafic intrusion belt, which consists of nearly three hundred intrusions, is distributed along the northern margin of the NCC (Chen et al., 1996; Tian et al., 2007). In the vicinity of Chicheng County, more than 120 ultramafic intrusions were tectonically emplaced into the Hongqiyingzi Complex, a metamorphosed complex mainly composed of amphibolite facies metavolcanic and metasedimentary rocks with Neoarchean to Paleoproterozoic ages (2535–2480 Ma, Liu et al., 2007). Retrograde eclogites can be found along the Jining–Chicheng–Pingquan major fault (Ni et al., 2004 and 2006). Recently Zhang et al. (2016) reported ca. 1.95 Ga U-Pb age for metamorphic zircons from the Hongqiyingzi Group, the country rock which hosts the retrograde eclogite. This metamorphic age places a Paleoproterozoic age constraint on the subduction to ecologite facies of our study area.

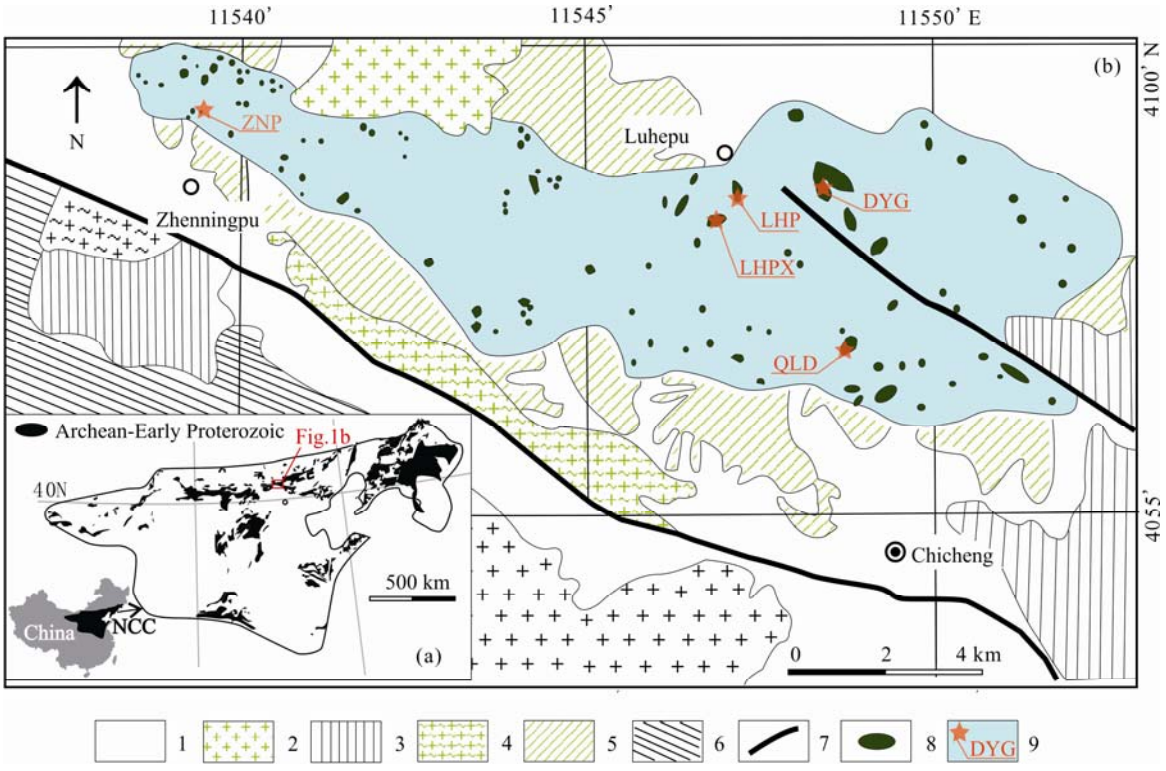


Fig. 1. (a), Location of the study area in the North China Craton. Distribution of Archean-Early Proterozoic geological units after Peng et al. (2010); (b), Simplified geological map of mafic-ultramafic bodies around Chicheng Country, North Hebei Province, China.
(1), Quaternary alluvium; (2), Yanshanian alkaline granite; (3), Jurassic volcanic rocks; (4), granitic gneiss-mylonite; (5), Early Proterozoic Hongqiyingzi complex; (6), Dantazi complex; (7), major fault; (8), ultramafic intrusions; (9), sample location and sample name.

The studied peridotites as well as boninite-like rocks occur as small blocks with outcrop lengths ranging from several hundreds of meters to five kilometers (Chen et al., 1996). No contact-metamorphic aureoles have been found between the peridotites and their wall rocks, implying that they are tectonically emplaced, ultramafic diapirs rather than intrusive magmatic bodies. Two boninite-like samples are from outcrops close to the Zhenningpu County, which are closely related to the peridotites (Fig. 1).

All the samples have experienced alteration due to post-emplacement hydrothermal reactions and surface weathering. Most of the olivine and orthopyroxene within the peridotites has been replaced by serpentine or talc, with the exception of sample LHPX01 (Fig. 2a–b). The undulating extinction of some of the large orthopyroxene porphyroclasts suggests that the peridotites have experienced ductile deformation (Fig. 2c).

In contrast to the olivine and opx, the spinel within the peridotites is well preserved. Most spinels are small, anhedral grains occurring along the boundaries of the major minerals (Fig. 2d). Clinopyroxene is absent in all peridotite samples. The boninite-like samples have the metamorphic mineral assemblage of tremolite+quartz+ chlorite+minor apatite (Fig. 2e–f).

3 Analytical Methods

We conducted mineral chemistry, major and trace element analyses, and Re-Os isotope analyses for the samples as described below.

3.1 Mineral chemistry

Mineral chemical compositions were analyzed using a JXA-8100 electron probe microanalyzer (EPMA) at Peking University in wavelength dispersive mode with 15 kV acceleration potential, 10 nA beam current and a beam diameter of 1 μm. Matrix corrections were applied using the PRZ correction program. 53 analytical standard minerals from American company SPI were used for external accuracy quantification, and mineral formulae were calculated based on stoichiometry. The analyzed olivine, orthopyroxene and spinel data are listed in Table 1 –3, respectively.

3.2 Major and trace element analysis

Major element analyses of bulk rock powers were conducted by X-Ray Fluorescence Spectrometry on fused glass disks using a Philips Avant (No.6735) + XRF-1500 instrument at the Laboratory of Orogenic and Crustal Evolution, Ministry of Education, Peking University.

Trace element concentrations were determined using a PerkinElmer Sciex ElAN 6000 ICP-MS. The USGS and Chinese National standards BHVO-2 and GSR-2 were chosen for element concentration calibration. Analytical uncertainties of REE and other incompatible element analyses are generally better than 5%.

All analyzed data are listed in Table 4.

Table 1 Composition of olivine from peridotite samples

Sample	LHPX01-01	LHPX01-05	LHPX01-06	05LHP01-1	05LHP01-2	05LHP4-1	05LHP04-5	05LHP04-7
SiO_2	41.15	40.63	41.00	41.27	41.13	41.27	40.83	41.73
TiO_2	0.03	0.00	0.04	0.03	0.00	0.04	0.01	0.00
Al_2O_3	0.00	0.00	0.01	0.02	0.00	0.00	0.00	0.00
FeO	8.75	8.54	8.38	8.77	8.76	7.96	7.81	7.59
MnO	0.17	0.10	0.14	0.11	0.14	0.13	0.12	0.07
MgO	49.93	49.87	50.12	49.52	49.77	51.06	50.12	51.14
CaO	0.01	0.00	0.01	0.01	0.00	0.03	0.02	0.08
Na_2O	0.01	0.01	0.00	0.01	0.00	0.00	0.03	0.00
K_2O	0.01	0.02	0.01	0.00	0.00	0.00	0.03	0.00
Cr_2O_3	0.00	0.00	0.00	0.02	0.02	0.03	0.00	0.00
NiO	0.40	0.35	0.32	0.39	0.36	0.38	0.41	0.37
Total	100.46	99.52	100.03	100.15	100.18	100.90	99.38	100.98
molecular formula (based on four oxygens and Fe^{3+}corrected)								
si	1.00	0.99	1.00	1.01	1.00	1.00	1.00	1.00
Ti	0.00	0.00	0.00	0.00	0.00	0.00	0.00	0.00
Al	0.00	0.00	0.00	0.00	0.00	0.00	0.00	0.00
Fe	0.18	0.17	0.17	0.18	0.18	0.16	0.16	0.15
Mn	0.00	0.00	0.00	0.00	0.00	0.00	0.00	0.00
Mg	1.82	1.83	1.83	1.80	1.81	1.84	1.83	1.83
Ca	0.00	0.00	0.00	0.00	0.00	0.00	0.00	0.00
Na	0.00	0.00	0.00	0.00	0.00	0.00	0.00	0.00
K	0.00	0.00	0.00	0.00	0.00	0.00	0.00	0.00
Cr	0.00	0.00	0.00	0.00	0.00	0.00	0.00	0.00
Ni	0.01	0.01	0.01	0.01	0.01	0.01	0.01	0.01
Total	3.00	3.01	3.00	2.99	3.00	3.00	3.00	3.00
$X_{Ol/Fe} = Fe^{2+}/(Mg + Fe^{2+})$	0.09	0.09	0.08	0.09	0.09	0.08	0.08	0.08
$X_{Ol/Mg} = Mg/(Mg + Fe^{2+})$	0.91	0.91	0.92	0.91	0.91	0.92	0.92	0.92

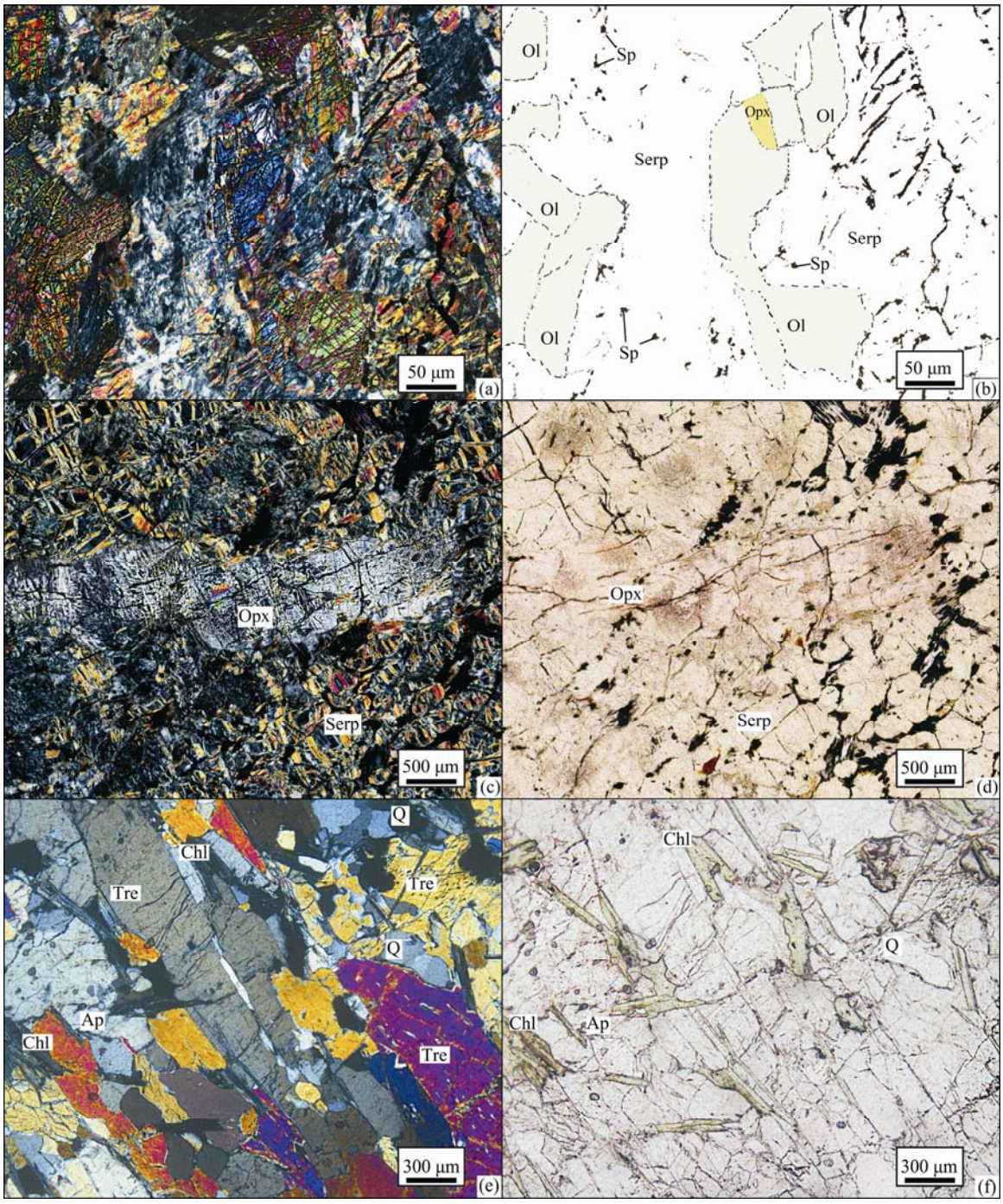


Fig. 2. Microphotographs of the North Hebei peridotites and boninitic rocks.
(a), Slightly serpentinized peridotite LHPX01, showing unserpentenized olivine (II to III interference) and orthopyroxene (I grey interference); (b), Cartoon color illustration of (a) under single polar: pale green represents olivine, yellow represents orthopyroxene, black represents chromian spinel and white represents serpentine; (c), unaltered orthopyroxene porphyroclast surrounded by serpentine under cross polar; (d), the same area of (c) under single polar, note the slightly reddish color of orthopyroxene and yellowish green color of serpentine. The serpentine grains are surrounded by opaque chromian spinels, which preserve the outline of the olivine grains before serpentinization. (e), metamorphic mineral assemblage (tremolite + quartz + chlorite + minor apatite) of ZNP-1, a sample with boninite-like chemical compositions, under cross polar; (f) single polar image of ZNP-1, showing the color and cleavage of chlorites.

3.3 Re-Os isotope analysis

Rhenium and Os isotope analyses were performed on bulk rock powders at the Institute of Geology and Geophysics, Chinese Academy of Science (IGGCAS) as per Shiry and Walker (1995). About 2 g of whole rock powder was added to a spike of mixed ^{185}Re and ^{190}Os, along with approximately 9ml of aqua regia. This was sealed inside Carius tubes, and heated at 240°C for 48–72 hours. After opening the tubes, the Os was extracted from the aqua regia solution into CCl_4 (Cohen et al., 1996) and

Table 2 Composition of orthopyroxene from peridotite samples

Sample	05LHP01-3	05LHP01-4	05LHP01-6	05LHP04-2	05LHP04-4
SiO_2	58.33	58.47	58.67	58.34	58.07
TiO_2	0.02	0.03	0.07	0.03	0.06
Al_2O_3	0.26	0.14	0.36	0.23	0.58
FeO	5.94	5.85	6.21	5.01	5.59
MnO	0.17	0.16	0.09	0.16	0.13
MgO	35.22	34.89	35.34	35.19	35.72
CaO	0.14	0.07	0.12	0.10	0.10
Na_2O	0.00	0.02	0.02	0.00	0.00
K_2O	0.00	0.03	0.01	0.02	0.00
NiO	0.06	0.07	0.02	0.00	0.11
Total	100.14	99.73	100.91	99.08	100.36
molecular formula (based on six oxygens and Fe^{3+}corrected)					
Si	2.00	2.01	2.00	2.01	1.98
Ti	0.00	0.00	0.00	0.00	0.00
Al	0.01	0.01	0.01	0.01	0.02
Cr	0.00	0.00	0.00	0.00	0.00
Fe^{3+}	0.02	0.02	0.02	0.02	0.02
Fe^{2+}	0.15	0.14	0.15	0.12	0.14
Mn	0.01	0.01	0.00	0.01	0.00
Mg	1.80	1.79	1.79	1.81	1.82
Ca	0.01	0.00	0.00	0.00	0.00
Na	0.00	0.00	0.00	0.00	0.00
K	0.00	0.00	0.00	0.00	0.00
Total	3.99	3.98	3.99	3.98	3.99

then back-extracted into HBr, followed by purification via microdistillation (Birck et al., 1997).

Rhenium was separated from the matrix and purified by anion exchange chromatography using 2 ml resin. The Re was further purified using a small anion exchange column packed with 0.1ml resin at the University of Maryland (UMD). All the collected fractions were dried down and re-dissolved in 1ml of 0.8 M HNO_3 for ICP-MS measurement.

Both Re and Os were corrected for blanks. Total blank levels were 8±2 and 3±2 pg for Re and Os respectively, and the blank $^{187}Os/^{188}Os$ ratio was 0.191±0.025. Precision of $^{187}Os/^{188}Os$ measurements, based on analysis of an in-house standard over a period of several months, was better than 0.4% (2σ). The analyzed data are listed in Table 5.

4 Results

4.1 Mineral chemistry

Compositions of olivine, orthopyroxene and spinel (Table 1–3) are described as below.

4.1.1 Olinine

The olivines from the peridotite samples have forsterite content ranging from Fo_{91} to Fo_{92} and NiO content from 0.35wt%–0.41wt%, typical of mantle peridotites (Frey et al., 1978). CaO content of the olivine ranges from 0.01Wt%–0.08wt%.

4.1.2 Orthopyroxene

The enstatite proportion of orthopyroxene ranges from 92.3% to 93.6%, with Al_2O_3, CaO and TiO_2 contents ranging from 0.14wt%–0.58wt%, 0.07wt%–0.14wt% and 0.02wt%–0.07wt%, respectively.

4.1.3 Spinel

In the spinel prism classification diagram (Deer et al., 1992), the spinels within the peridotites are plotted over the chromite, Al-chromite, picotite and hercynite areas (Fig. 3b). In the Cr_2O_3 vs. Al_2O_3 diagram (Fig. 4), the samples are distributed along a linear array from a high Cr chromite end member (Cr_2O_3 = 45wt%–60wt%) to a high Al chromite end member (Al_2O_3>25wt%). This is typical in chromite of magmatic origin (Zhou et al., 2014) and residual mantle spinels (Morten et al., 1989; Hao et al., 2013; Himmelberg et al., 1973), respectively. The TiO_2 content of the spinels ranges from 0.02 wt%–0.76wt%. Fluid alteration can increase the Fe^{3+} and decrease the Al^{3+} of chromite (Baumgartner et al., 2013), so hydrothermally altered spinel will plot in the low-Al_2O_3 area, as shown in Fig. 4. Our spinel samples have no overlap with the "altered spinel" field in Fig. 4, confirming that they remain unaltered hydrothermally.

One analysis of spinel from the boninite-like sample is characterized by high Cr_2O_3 (54.63wt%), low Al_2O_3 (12.28wt%), and low TiO_2 (0.05wt %), thereby falling into the "Hercynite" field (Fig. 3c).

4.2 Major element geochemistry of whole rock

Major element compositions of whole rock samples are listed in Table 4. The peridotite samples are characterized by high loss-on-ignition (LOI) from 13.08wt% to 14.00wt%, due to pervasive serpentinization. When normalized to exclude volatile elements, the peridotites have Al_2O_3 (1.30wt%–2.07wt%), CaO (0.0–0.28wt%) and FeOt (5.57wt%–7.21wt%) lower than fertile peridotite, while MgO (41.9wt%–43.3wt%) and SiO_2 (46.7wt%–47.4wt%) are higher than fertile peridotite (Fig. 5). The boninite-like samples have high SiO_2 (53.91wt%–57.18wt%) and extremely low TiO_2 (0.059wt%–0.067wt%), typical of arc boninites.

4.3 Rare earth and trace elements

The REE abundances of the peridotites (Table 4) are plotted in a chondrite-normalized diagram and compared with modeled residual mantle peridotites at variable depth and melt fraction (Fig. 6). The peridotite samples have flat or slightly left-dipping heavy rare earth element (HREE) distribution and variably enriched light rare earth elements (LREEs). The peridotites display a small Europium anomaly (dEu), ranging from 0.70 to 1.70. Based on the variation in LREE enrichment, the REE patterns of the peridotites can be divided into two types: the "U-shape" patterns that are characterized by enrichment of La and

Table 3 Composition of spinel from peridotite samples

Sample	05LHP01-9	05LHP01-10	LHPX01-03	LHPX01-04	05LHP04-1	05LHP04-2	LHPX02-1	LHPX02-2	DYG01-1
Rock type	peridotite	peridotite	peridotite	peridotite	peridotite	peridotite	peridotite	peridotite	peridotite
TiO_2	0.00	0.03	0.07	0.09	0.15	0.15	0.01	0.06	0.50
Al_2O_3	48.43	50.55	34.89	35.50	12.51	14.44	32.77	10.15	8.63
Cr_2O_3	18.83	17.52	31.60	33.62	54.27	51.69	34.92	59.15	56.25
Fe_2O_3	1.96	1.96	1.57	1.44	3.67	4.25	2.08	1.20	3.06
FeO	11.10	11.09	16.65	15.92	22.43	22.22	16.24	22.37	24.72
MnO	0.15	0.09	0.19	0.24	0.40	0.43	0.46	0.37	0.88
MgO	17.59	18.23	13.64	14.21	7.55	7.91	13.99	6.99	5.26
Total	98.06	99.47	98.61	101.02	100.98	101.09	100.47	100.29	99.30
Molecular formula (based on four oxygens and Fe^{3+}corrected)									
Ti	0.00	0.00	0.00	0.00	0.00	0.00	0.00	0.00	0.01
Al	1.56	1.60	1.21	1.20	0.49	0.56	1.12	0.40	0.35
Cr	0.41	0.37	0.73	0.76	1.41	1.33	0.80	1.57	1.54
Fe^{3+}	0.04	0.04	0.04	0.03	0.09	0.10	0.05	0.03	0.08
Fe^{2+}	0.25	0.25	0.41	0.38	0.62	0.61	0.40	0.63	0.72
Mn	0.00	0.00	0.01	0.01	0.01	0.01	0.01	0.01	0.03
Mg	0.72	0.73	0.60	0.61	0.37	0.38	0.61	0.35	0.27
$Mg^{\#}$	0.74	0.75	0.59	0.61	0.38	0.39	0.61	0.36	0.26
$Cr^{\#}$	0.21	0.19	0.38	0.39	0.74	0.71	0.42	0.80	0.81
Al_2O_{3mdt}	18.34	18.52	16.98	17.06	14.33	15.07	16.72	13.23	12.38
TiO_{2melt}	- 0.84	- 0.84	- 0.24	- 0.06	0.25	0.25	- 1.62	0.15	0.63
mg Ol	0.91	0.91	0.91	0.91	0.92	0.92			
T1	1005.69	1004.14	895.59	929.70	882.89	877.71			
T2	1038.46	1034.46	939.49	976.55	942.68	934.92			
f_{O2}(FMQ)	–0.27	–0.22	–0.63	–0.96	0.70	0.97			

Sample	DYG01-2	DYG01-3	DYG01-4	QLD02-10	QLD02-2	QLD02-3	QLD02-4	QLD02-7	QLD02-8	QLD02-9
Rock type	peridotite	peridotite	peridotite	peridotite	peridotite	peridotite	peridotite	peridotite	peridotite	peridotite
TiO_2	0.38	0.14	0.14	0.20	0.30	0.13	0.76	0.10	0.07	0.21
Al_2O_3	8.48	9.46	10.83	11.14	11.12	12.65	4.95	12.52	12.16	12.20
Cr_2O_3	56.63	57.51	56.49	55.53	54.27	55.62	60.64	54.65	55.67	56.09
Fe_2O_3	3.66	2.25	2.25	2.63	3.95	1.69	3.53	2.70	2.54	1.39
FeO	24.01	23.45	22.71	23.11	23.22	22.04	22.61	21.33	22.27	21.74
MnO	0.78	0.72	0.74	0.67	0.58	0.59	0.75	0.58	0.66	0.67
MgO	5.53	6.13	6.82	6.47	6.68	7.64	6.34	7.71	7.16	7.76
Total	99.47	99.66	99.98	99.75	100.12	100.36	99.58	99.59	100.53	100.06
Molecular formula (based on four oxygens and Fe^{3+}corrected)										
Ti	0.01	0.00	0.43	0.01	0.01	0.00	0.02	0.00	0.00	0.01
Al	0.35	0.38	1.51	0.44	0.44	0.49	0.20	0.49	0.48	0.48
Cr	1.54	1.55	0.06	1.48	1.44	1.46	1.67	1.44	1.46	1.47
Fe^{3+}	0.10	0.06	0.64	0.07	0.10	0.04	0.09	0.07	0.06	0.04
Fe^{2+}	0.69	0.67	0.02	0.65	0.65	0.61	0.66	0.59	0.62	0.60
Mn	0.02	0.02	0.34	0.02	0.02	0.02	0.02	0.02	0.02	0.02
Mg	0.28	0.31	0.00	0.33	0.34	0.38	0.33	0.38	0.35	0.38
$Mg^{\#}$	0.27	0.30	0.33	0.31	0.31	0.37	0.31	0.37	0.34	0.38
$Cr^{\#}$	0.82	0.80	0.78	0.77	0.77	0.75	0.89	0.75	0.75	0.76
Al_2O_{3mdt}	12.29	12.86	13.57	13.72	13.71	14.38	9.48	14.33	14.18	14.19
TiO_{2melt}	0.50	0.24	0.24	0.31	0.42	0.23	0.92	0.20	0.17	0.32
mg Ol										
T1										
T2										
f_{O2}(FMQ)										

Sample	ZNP01-4	05LHP02-1	05LHP02-2	05LHP02-3	05LHP02-4	05LHP02-5	05LHP02-6	05LHP02-7	05LHP02-8
Rock type	boninite-like	peridotite	peridotite	peridotite	peridotite	peridotite	peridotite	peridotite	peridotite
TiO_2	0.05	0.19	0.08	0.05	0.13	0.10	0.07	0.02	0.03
Al_2O_3	12.28	11.49	26.35	14.49	28.35	19.70	24.10	21.43	31.07
Cr_2O_3	54.63	55.20	39.86	53.16	39.13	47.48	42.81	46.15	37.21
Fe_2O_3	0.00	2.53	2.37	2.48	1.70	2.38	2.09	2.41	1.87
FeO	28.69	22.56	19.20	21.93	18.42	21.00	19.62	19.69	18.22
MnO	1.11	0.63	0.46	0.74	0.52	0.65	0.53	0.58	0.55
MgO	1.67	6.97	10.52	7.74	11.52	8.91	10.18	10.00	12.01
Total	98.43	99.57	98.84	100.59	99.77	100.22	99.40	100.28	100.96
Molecular formula (based on four oxygens and Fe^{3+}corrected)									
Ti	0.00	0.01	0.00	0.00	0.00	0.00	0.00	0.00	0.00
Al	0.50	0.46	0.96	0.56	1.02	0.74	0.89	0.79	1.09
Cr	1.51	1.47	0.98	1.38	0.94	1.20	1.06	1.15	0.87
Fe^{3+}	0.00	0.06	0.06	0.06	0.04	0.06	0.05	0.06	0.04
Fe^{2+}	0.84	0.64	0.50	0.60	0.47	0.56	0.51	0.52	0.45
Mn	0.03	0.02	0.01	0.02	0.01	0.02	0.01	0.02	0.01
Mg	0.09	0.35	0.49	0.38	0.52	0.42	0.48	0.47	0.53
$Mg^{\#}$	0.09	0.34	0.47	0.37	0.51	0.41	0.46	0.45	0.52
$Cr^{\#}$	0.75	0.76	0.50	0.71	0.48	0.62	0.54	0.59	0.45
Al_2O_{3mdt}	14.23	13.88	15.82	15.09	16.12	16.70	15.45	14.97	16.50
TiO_{2melt}	0.14	0.30	–0.14	0.14	0.20	0.20	- 0.24	- 1.13	- 0.84
mg Ol									
T1									
T2									
f_{O2}(FMQ)									

Note: Al_2O_3 and TiO_2 compositions of melt in equilibrium with the spinels are calculated according to the regression of Kamenetsky et al. (2001); *mg* Ol are averaged Mg/[Mg+Fe^{2+}] of coexisting olivine from Table 1; T1 and T2 are temperatures after the calibrations of Ballhaus et al.(1991) and O'Neill and Wall (1987), respectively; fO_2 values were calculated after Ballhaus et al.(1991).

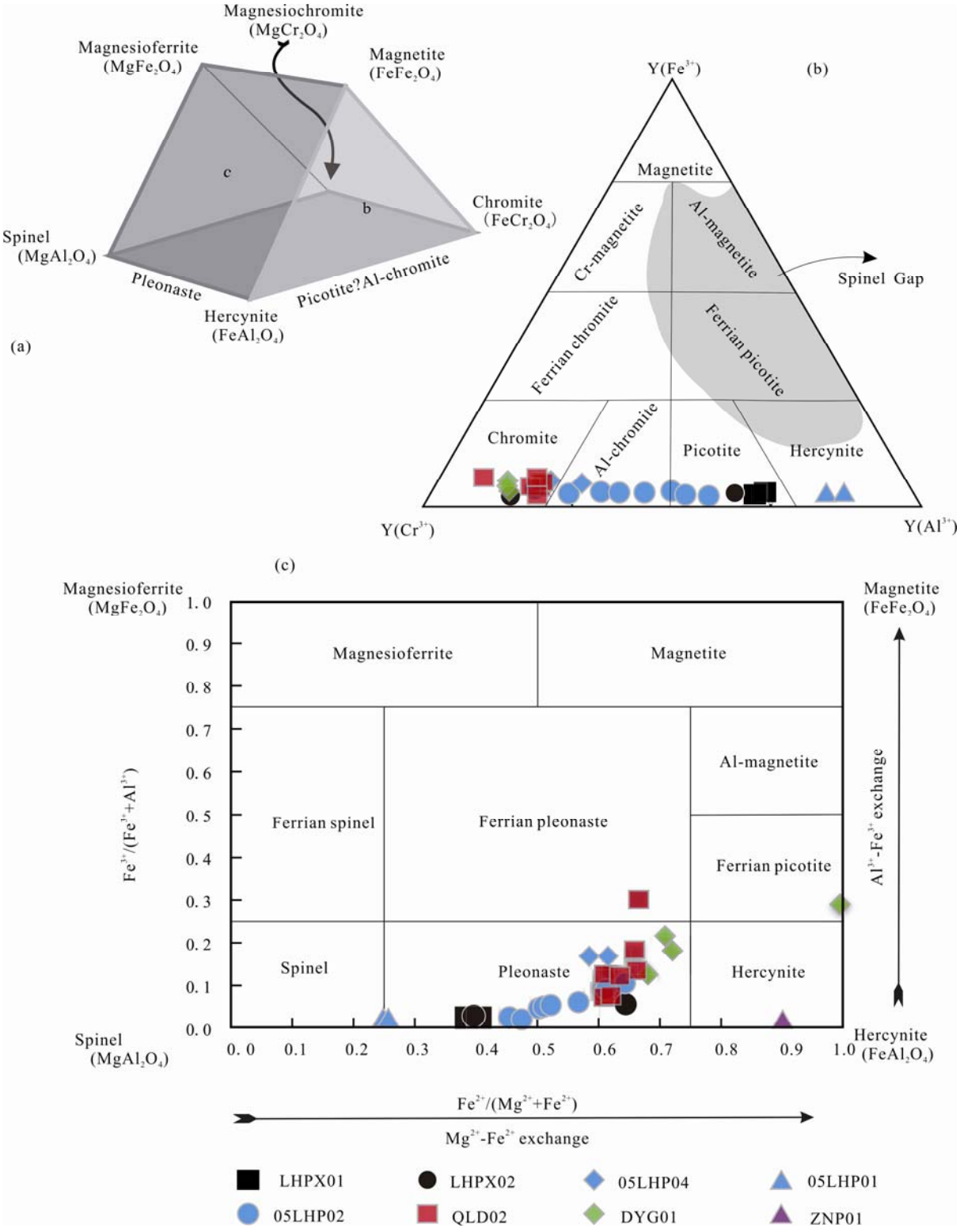


Fig. 3. Chemical classification diagrams for the spinel group minerals.
(a), Spinel prism for the multi-component system after Deer et al. (1992). The letter "b" indicated in the triangular-front face and the letter "c" in the lateral-left face of the prism, represent the diagrams in (b) and (c) respectively. (b), Triangular classification diagram. $Y(Cr^{3+}) = Cr/(Cr+Fe^{3+}+Al)$; $Y(Fe^{3+}) = Fe^{3+}/(Cr+Fe^{3+}+Al)$; $Y(Al^{3+}) = Al/(Cr+Fe^{3+}+Al)$. "Spinel gap" field is from Barnes and Roeder (2001). (c), Binary classification diagram considering the Mg^{2+}-Fe^{2+} exchange in the structural site "X": $Fe^{2+}/(Mg^{2+}+Fe^{2+})$. Field-contours in both diagrams are considering Stevens (1944), Haggerty (1991) and Deer et al. (1992).

Ce, with a trough at Nd and Sm; and the "sinusoidal type" patterns which are characterized by highly enriched light and middle REE up to Dy (Fig. 6).

The boninite-like samples have low Nb/La ratios (0.09–

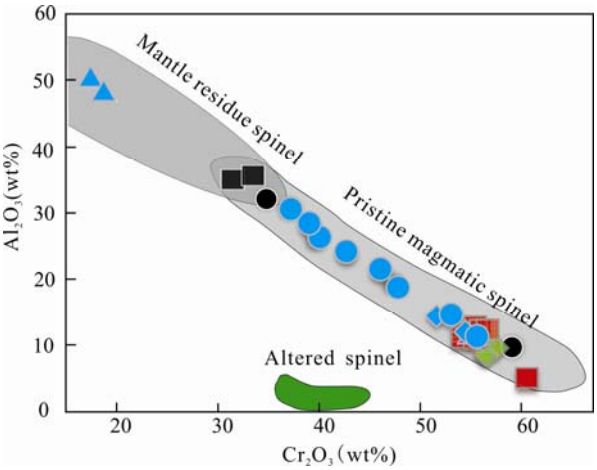


Fig. 4. Plot of Cr_2O_3 vs Al_2O_3 of spinels from the samples.
The grey area represents unaltered chromite (Zhou et al., 2014) while the brown area represents altered chromite (Zhou et al., 2014). The mantle spinel data are from Morten et al. (1989); Hao et al. (2013) and Himmelberg et al. (1973). Legend as in Fig. 3.

0.42) and low $(Zr/Sm)_{PM}$ ratios (0.05–0.80)- typical of arc boninites- and their Ti/Zr ratios (12–184) and Zr contents are similar to the Archean second stage melts (Smithies et al., 2004). The Sc abundance of the boninite-like samples is much lower than that of the Archean second stage melts; however, Sc is easily lost during submarine alteration (Staudigel and Hart, 1983). Therefore, the low Sc abundance may not be a characteristic of the magma but the fingerprint of later alteration. REEs in boninitic rocks however, are relatively immobile and would not be greatly affected by post magmatic alteration. In Fig. 7, the boninite-like samples are compared with different types of the Archean second-stage melts (Whundo- and Whitney-type from Smithies et al., 2004). Their low La/Yb and La/Gd ratios are identical to the subduction-related Whundo-type boninites, but higher than the plume-related Whitney-type.

4.4 Re-Os isotopical geochemistry

Rhenium and Os isotopic data are reported in Table 5. The abundance of Osmium in the peridotites varies from 2.9 ppb to 4.6 ppb, while the boninite-like samples have a smaller range from 1.5 ppb to 2.1 ppb. The $^{187}Os/^{188}Os$ ratios of the peridotites range from 0.113 to 0.122, yielding T_{RD} from 981Ma to 2054 Ma (Table 5). The boninite-like samples also have low $^{187}Os/^{188}Os$ ratios of 0.1164 and 0.1220.

5 Discussion

5.1 Mantle melt depletion and metasomatism of peridotites

The presence of high-Al residual mantle spinels in peridotite samples (Fig. 4) suggests that the peridotites

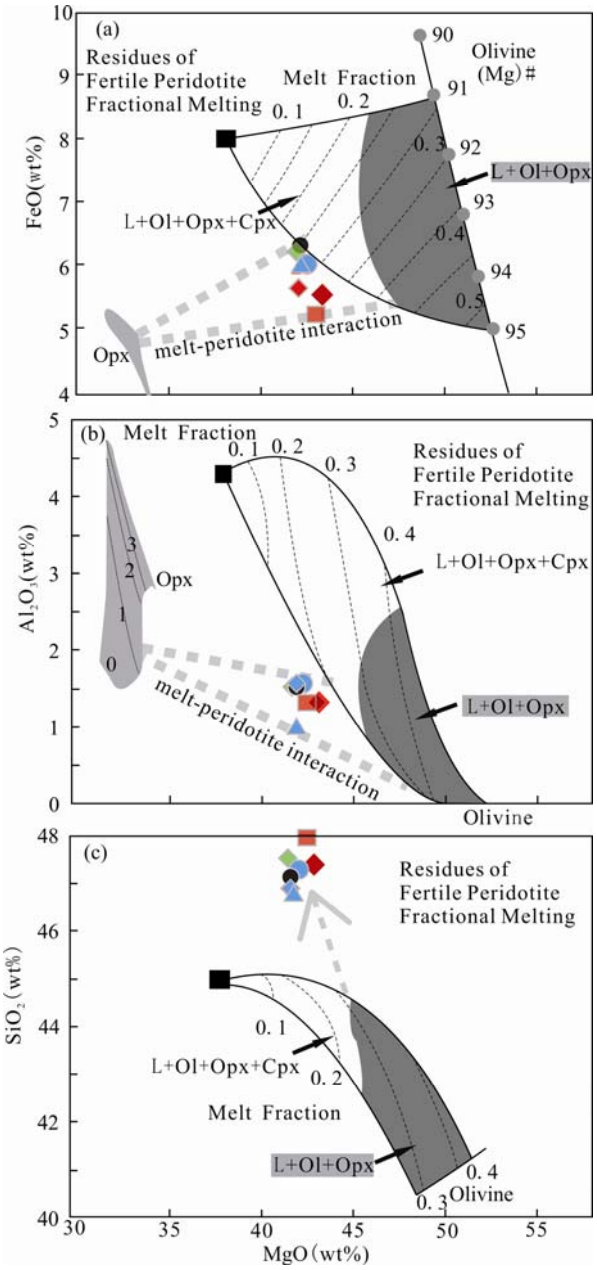


Fig. 5. Major element compositions of the peridotites from North Hebei with comparisons to experimentally determined melting trajectories of model fertile peridotite: (a) FeO-MgO, (b) Al_2O_3-MgO and (c) SiO_2-MgO.
Model residue compositions formed by fractional melting of fertile peridotite KR-4003 (Herzberg, 2004). Orthopyroxene compositions are from Herzberg and O'Hara (2002) for liquids in equilibrium with harzburgite at the pressures (GPa) indicated. Legendkey as in Fig. 3.

come from the lithospheric mantle. This means we can use these peridotites to make inferences about melting in the NCC lithospheric mantle. Partial melting will preferentially remove the clinopyroxene component from the mantle source into a melt (Walter, 2003), and therefore the mineral proportions of peridotites can be used to evaluate the degree of mantle melt depletion. Unfortunately, most of our peridotite samples have experienced alteration, and most

Table 4 Bulk rock chemical compositions of peridotites and boninite-like rocks

Sample	DYG01	05LHP01	05LHP02	05LHP04	LPHX02	QLD01	QLD02	ZNP01	ZNP02
Rock(wt%)	peridotite	peridotite	peridotite	peridotite	peridotite	peridotite	peridotite	Boninite-like	Boninite-like
SiO_2	40.68	40.07	40.73	40.60	40.26	40.52	41.21	57.18	53.91
TiO_2	0.022	0.019	0.016	<0.010	<0.010	<0.010	<0.010	0.059	0.067
Al_2O_3	1.30	1.77	1.34	1.37	1.29	1.12	1.12	3.74	3.71
Fe_2O_3T	7.10	6.88	6.86	6.44	7.21	6.30	6.02	5.94	5.57
MnO	0.096	0.11	0.064	0.10	0.078	0.094	0.12	0.26	0.15
MgO	35.93	36.15	36.64	36.42	36.02	37.06	36.93	19.45	19.59
CaO	0.11	0.23	0.086	0.24	0.18	<0.010	0.029	10.58	11.20
Na_2O	<0.010	<0.010	<0.010	<0.010	<0.010	<0.010	<0.010	0.32	0.17
P_2O_5	0.008	<0.004	<0.004	<0.004	0.006	<0.004	<0.004	0.006	<0.008
LOI	14.00	13.42	13.08	13.96	13.66	13.56	13.58	1.92	4.26
Total	99.25	98.65	98.82	99.13	98.70	98.65	99.01	99.46	98.63
	ppm								
Sc	6.227	7.675	5.53	6.735	7.052	8.464	7.16	2.956	2.899
Ti	104.9	63.36	51.78	38.75	52.2	39.47	30.68	290.4	282.6
V	30.56	37.44	30.4	31.81	37.28	38.24	33.46	28.39	29.25
Cr	2188	2403	2472	2869	2794	3345	2932	1377	1936
Co	88.97	97.83	107	99	103.9	102.7	104.2	45.87	47.89
Ni	1610	1886	2214	1730	2066	1791	1949	861	959
Cu	2.401	0.504	0.566	1.853	1.85	0.043	0.654	0.446	0.042
Zn	35.35	35.37	30.99	32.87	41.74	38.1	36.96	61.25	71.34
Ga	0.82	1.12	0.89	0.71	0.79	0.79	0.71	5.25	5.96
Ge	0.772	0.097	0.87	0.848	0.981	0.648	0.146	1.818	1.914
Rb	0.178	0.412	0.074	0.141	0.179	0.153	0.093	0.586	0.554
Sr	3.362	8.792	2.665	5.898	1.616	0.738	0.897	40.6	30.81
Y	0.483	0.439	0.202	0.304	0.42	0.254	0.127	6.348	5.92
Zr	1.276	0.319	0.20	0.157	0.128	0.179	0.351	1.579	23.49
Nb	0.117	0.105	0.065	0.082	0.039	0.042	0.031	0.625	0.392
Ba	3.991	13.00	21.61	3.764	3.425	0.567	0.883	2.48	2.65
Hf	NA	NA	NA	NA	NA	NA	NA	0.043	0.659
Ta	NA	NA	NA	NA	NA	NA	NA	0.056	0.026
Pb	0.176	0.362	0.299	0.114	0.523	0.199	0.442	0.978	1.19
Th	0.07	0.07	0.06	0.06	0.05	0.08	0.07	0.12	1.59
U	0.743	0.012	0.03	0.098	7.958	0.012	0.018	0.151	0.619
	ppb								
La	310.5	114.6	78.76	141.7	64.55	237.3	194.5	1500	4528
Ce	875.1	237.9	133.3	261.0	155.2	778.6	617.2	5488	10230
Pr	144.5	28.78	17.04	29.40	19.56	148.5	101.0	932	1293
Nd	690.8	116.2	65.53	107.2	88.23	724.6	477.7	4270	5310
Sm	150.3	28.54	10.35	23.84	31.70	158.0	82.80	1183	1171
Eu	41.78	16.45	5.683	9.863	19.35	28.46	27.45	1172	463
Gd	122.9	30.29	16.31	26.71	42.85	97.45	59.1	1024	1117
Tb	17.57	8.570	3.493	6.949	8.183	14.08	4.769	185	183
Dy	90.48	71.13	32.31	45.89	62.38	54.52	22.74	1090	1089
Ho	18.68	18.05	7.633	13.02	16.51	11.26	5.045	208	216
Er	62.12	59.31	27.99	43.76	57.15	33.63	15.91	601	626
Tm	8.714	10.43	4.892	6.506	8.661	4.604	2.849	106	89
Yb	53.48	70.75	41.32	53.72	70.28	33.82	24.53	727	609
Lu	9.406	10.16	8.067	10.04	13.35	6.591	4.002	120	86

Table 5 Re-Os isotopic and composition data for peridotites and boninite-like rocks

Sample	Re conc. (ppt)	Os conc. (ppt)	$^{187}Os/^{188}Os$	2sigma	$^{187}Re/^{188}Os$	T_{RD}(Ma)	T_{MA}(Ma)
ZNP01	27.68	1456.48	0.1164	0.000040	0.0546	1565.83	1808.50
ZNP02	12.09	2051.94	0.1220	0.000057	0.0170	747.53	780.25
DYG01	9.98	3515.76	0.1154	0.000034	0.0082	1714.02	1749.04
QLD01	17.49	3664.23	0.1134	0.000034	0.0137	1999.38	2068.81
QLD02	5.27	3315.20	0.1139	0.000026	0.0046	1927.65	1949.45
05LHP01	12.30	3786.15	0.1193	0.000096	0.0093	1143.92	1170.89
05LHP02	2.09	2906.62	0.1130	0.000016	0.0021	2054.84	2065.27
05LHP04	16.81	4621.23	0.1196	0.000035	0.0105	1100.67	1129.81
LHPX02	16.79	3421.59	0.1204	0.000079	0.0141	981.15	1016.56

Note: All the reported values have been corrected for mass fractionation and blank (Re = 8±2 pg, and Os = 3±2 pg); The parameters used in the calculation are: $\lambda_{Re} = 1.666\times10^{-11}$/year (Smoliar et al., 1996), $(^{187}Re/^{188}Os)_{Chond} = 0.40186$,$(^{187}Os/^{188}Os)_{Chond,0} = 0.1270$ (Shirey and Walker, 1998).

primary minerals have been replaced by secondary minerals such as serpentine, talc, and bastite. As a result, the original mineral compositions of the peridotites must be estimated by modal mineral calculations from bulk rock compositions. We use the volatile-free major element data to calculate the modal mineral composition of the peridotites using the thermodynamic simulation software THERMOCALC ver.3.33. The specified mineral activity models used in the calculation are as follows: (1) Clinopyroxene from Green et al. (2007); (2) Garnet from

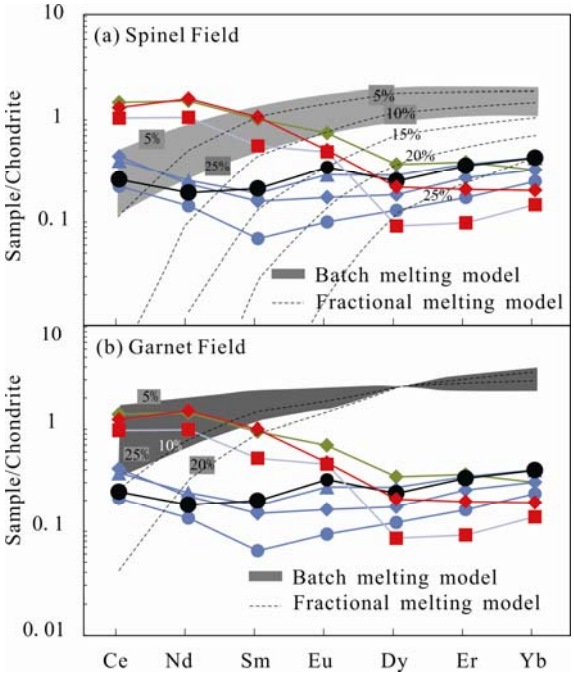


Fig. 6. Chondrite-normalized rare earth element diagrams of the peridotites from North Hebei in comparison to REE patterns of residual mantle modelled in (a) the spinel stability field and (b) the garnet stability field.
The starting mantle compositions, partition coefficients and fractional melting models are from Johnson et al. (1990).

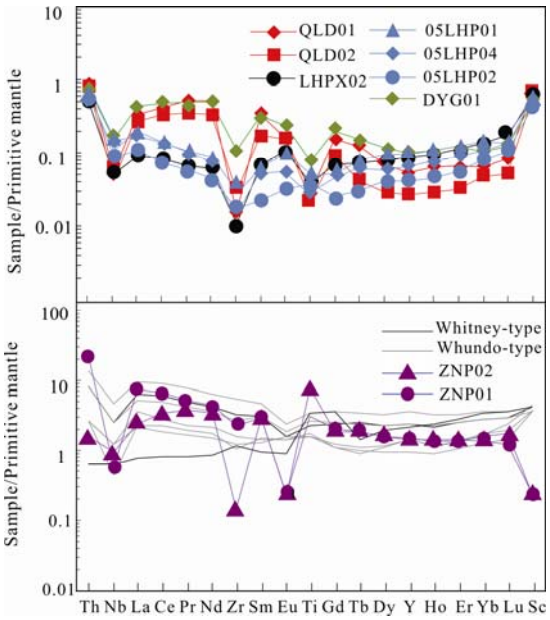


Fig. 7. Primitive mantle (PM)-normalized trace element diagrams for peridotite samples (a) and boninite -like samples (b) (ZNP01 and ZNP02).
PM values are from Sun and McDonough (1989). The thin grey and thick black lines represent the Whundo-type and Whitney-type boninites from Smithies et al. (2004) and Kerrich et al. (1998), respectively.

White et al. (2007); (3) Orthopyroxene from Powell and Holland (1999); (4) Spinel from Powell and Holland (1998), and an ideal mixing model is used for the olivine activity.

The modal mineral compositions calculated at the spinel and garnet stability depth are listed in Table 6. It is clear that the peridotites are extremely low in modal clinopyroxene abundance. If calculated at the spinel stability depth, the modal clinopyroxene ranges from 0.06wt%–1.13wt%; however, if calculated at the garnet stability depth, the modal clinopyroxene decreases to 0.04wt % –0.64wt %. These extremely low modal clinopyroxene abundances suggest that the peridotites were highly refractory harzburgites before serpentinization. The absence of clinopyroxene in petrographic observation (as shown in Fig. 1) also suggests that the peridotites from North Hebei Province were likely to be harzburgites.

The major element compositions of the peridotites were plotted in FeO, Al_2O_3 and SiO_2 V.S. MgO diagrams (Fig. 5a, b and c) and compared with experimentally determined melt depletion trajectories (Herzberg, 2004). It is clear that the peridotite samples have MgO contents much higher than primitive fertile mantle as represented by KR-4003 (Fig. 5). Actually, the olivine Fo contents (91–92) of the peridotites correspond to melt depletion rates of ~30% or higher (Fig. 5a). In terms of Al_2O_3, the peridotite samples plot close to the melt depletion trajectory of ~20%, although their MgO contents are slightly lower. This can be explained by the addition of SiO_2 (orthopyroxene), which may lower the MgO contents of the bulk rock compositions. If we take the addition of orthopyroxene into account, the original melt depletion ratios can be constrained by connecting the orthopyroxene endmember, the peridotite samples, and the melt depletion trajectories. As shown in Fig. 5a and 5b, the "melt-peridotite interaction" lines passing through the orthopyroxene field and the North Hebei peridotite samples will intersect the ~20% to ~30% melt depletion trajectories. This is consistent with the nearly clinopyroxene-absent petrography and the extremely low clinopyroxene modal compositions (Table 6). Actually, the fertile mantle source KR-4003 contains over 27wt% clinopyroxene at garnet stability pressures (Walter, 1998), and therefore forming harzburgites within the garnet stability field would require the complete removal of the ≥27wt% clinopyroxene. In the spinel stability field the clinopyroxene abundance should be higher because decomposition of garnet will yield new clinopyroxene (Johnson et al., 1990) and a higher degree of melting would be required for generating harzburgites.

In Fig. 5a–b the addition of orthopyroxene is evidenced by the shifting of peridotite sample points from the melt-residue area toward the orthopyroxene field. In the MgO-SiO_2 co-variation diagram (Fig. 5c), the peridotites form a remarkable SiO_2-enrichment trend. Orthopyroxene-rich peridotites are found in cratonic mantle and active subduction zones (Herzberg, 2004), both of which can be

Table 6 The model compositions calculated with ThermoCalc for spinel stability depth and garnet stability depth

Sample	DYG01	05LHP01	05LHP02	05LHP04	LPHX02	QLD01	QLD02
rock	peridotite	peridotite	peridotite	peridotite	peridotite	peridotite	peridotite
at 900℃ 20kBar							
di	0.26	0.35	0.18	0.65	0.45	0.05	0.13
gt	2.11	5.02	2.30	2.75	2.52	0.51	0.52
opx	43.01	37.60	41.12	41.04	40.21	41.95	45.27
ol	54.62	57.03	56.40	55.57	56.83	57.49	54.09
at 600℃ 10kbar							
di	0.54	1.09	0.43	1.13	0.86	0.06	0.17
opx	44.79	41.75	43.11	43.23	42.25	42.43	45.73
sp	1.11	2.01	1.20	1.26	1.16	0.84	0.73
ol	53.56	55.15	55.26	54.38	55.72	56.67	53.37

interpreted as reaction products of residual mantle with a silica-rich melt (Kelemen et al., 1992, 1998). These two types can be distinguished using MgO–FeO_T systematics: orthopyroxene-rich cratonic mantle peridotites are FeO-depleted, while modern forearc peridotites with excess orthopyroxene often form FeO_T enrichment trends (Herzberg, 2004). In this case, the North Hebei peridotites display an FeO-depletion trend (Fig. 5a), suggesting a cratonic mantle origin rather than a modern arc-type origin.

5.3 Trace element systematics

The variable enrichment of light to middle REEs of the North Hebei peridotites is indicative of a post-melt depletion alteration event. Mantle metasomatism is common in peridotite xenolith samples which can result in enrichment of the light to middle REEs (e.g., Bodinier et al., 1990; Ionov et al., 2002; Chen et al., 2014). Before the possibility of mantle metasomatism can be discussed however, the influence of serpentinization on the trace element systematics of the North Hebei peridotites must be determined.

Remarkable compositional variations of REEs and trace elements have been reported in modern sea floor abyssal peridotites, which have a predominantly serpentine mineral assemblage. Based on the positive correlation between Th and REE, Niu (2004) and Paulick et al. (2006) suggest that the serpentinized peridotites can preserve their original REE systematics in high T regimes, and therefore the REE patterns can be used to evaluate the extent of mantle melt depletion and melt-peridotite interaction. More recent studies, however, have revealed that LREEs are mobile during interactions between hydrothermal fluids and serpentinites (Allen and Seyfried, 2005; Menzies et al., 1993). Based on a detailed review of global serpentinite geochemical data, Deschamps (2013) suggested that HREEs of serpentinized peridotites are poorly mobile and therefore they can retain the geochemical signature of the original protolith. In light of this we suggest that the highly immobile elements, like Nb, Th and HREEs, may be more reliable than other trace elements when making geochemical inferences about the mantle protolith.

In the Nb-La diagram (Fig. 8a), the North Hebei peridotites plot at the intersection of the fluid/rock and melt/mantle trajectories. This means that the processes that are responsible for the LREE enrichment of the peridotite samples cannot be identified. When the more immobile elements Th, Gd and Lu (Fig. 8b) are used, however, the North Hebei peridotites plot off the fluid/rock trend and close to the melt/mantle interaction trend. This proves that the HREEs were poorly mobile during serpentinization of the peridotites and their signatures have been preserved at high temperatures.

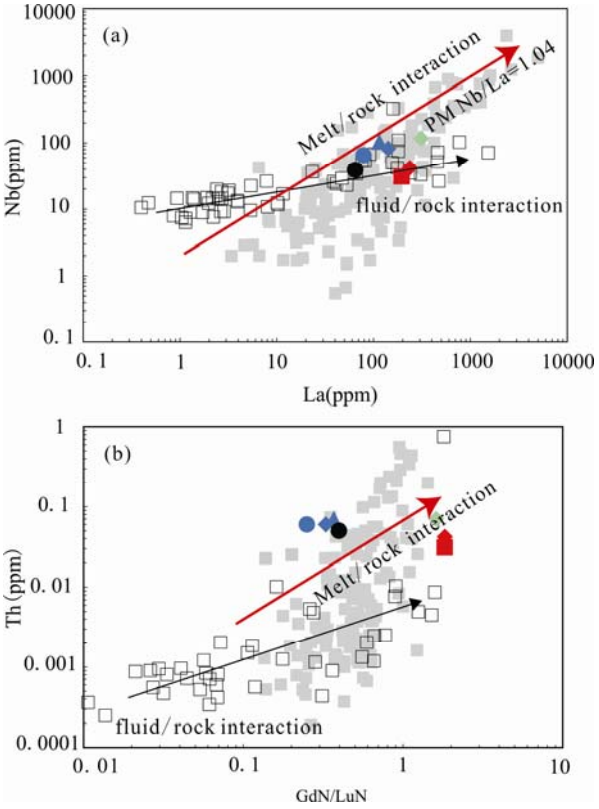


Fig. 8. Nb-La (a) and Th-GdN/LuN(b) diagrams for the North Hebei peridotites, showing comparisons with deviating trends for melt–mantle interaction and hydrothermal fluid/rock interaction.

PM Nb/La ratio is calculated using primitive mantle data from Sun and McDonough (1989). The grey squares are global abyssal peridotites compiled by Niu, (2004). The open squares are serpentites that have experienced fluid/peridotite interaction from Paulick et al. (2006).

In chondrite-normalized rare earth element diagrams (Fig. 6), the HREEs of the peridotites are much lower than PM values with flat to slightly left-dipping distributions. This suggests that the North Hebei peridotites have not experienced melt depletion in the garnet stability field, as existence of garnet in the melting residue would result in an elevation of HREE abundances, as well as a steeply left -dipping HREE distribution (Fig. 6b). Absence of an Eu anomaly also rules out the existence of plagioclase in the mantle source. Following the melt extraction model proposed by Johnson et al. (1990), we estimated that the studied peridotites have experienced melt extraction of more than 25% in the spinel stability field (Fig. 6a), while melting in the garnet stability field cannot match the HREE patterns of any of the samples (Fig. 6b). Although the stability of HREEs during serpentinization cannot be completely guaranteed, this melt extraction rate is consistent with the petrographic observation that clinopyroxenxe is absent, and major element constraints which show extremely low values of CaO and TiO_2.

It should be noted that the starting mantle composition in the REE modelling is fertile primitive mantle (Johnson et al., 1990), and consists of nearly 30% clinopyroxene at spinel and garnet stability pressures (Walter, 1998). For generating MORBs, the depleted mantle source peridotites were estimated to have experienced ~10% (Langmuir et al., 1992) to 15% melting (Niu and Batiza, 1991) at dry condition. A rather lower melting ratio was proposed (<6.5%) by Asimow and Langmuir (2003) when they assume that the solidus of peridotites was "dampened" by H_2O in nominally anhydrous minerals. However, the anhydrous solidus used in their parameterization has recently been disproved because earlier partial melting experiments failed to avoid H_2O adsorption onto starting materials (Sarafian et al., 2017). Therefore, a 10%–15% melting extent at the mid-ocean ridge area can be assumed.

At subduction zones, the already depleted mantle wedge can be melted by a flux of slab-derived fluids. The melting extent at subduction zones was estimated to be ~10% by different parameterization melting models (e.g., Katz and Langumir, 2003; Kimura et al., 2014). This means that if the first-stage melt depletion at ridges and second-stage flux melting of highly depleted mantle at subduction zones are combined, a total of 25% melt extraction is reasonable.

5.3 Mantle-derived melts in an arc setting

The magmatic spinels, including chromites, Al-chromites, and picotites, are resistant to weathering and alteration. Their mineral chemical compositions can be used to constrain the composition of their parental magma, which should represent the melt end-member during metasomatic processes. We calculated the Al_2O_3 and TiO_2 composition of melts (Table 3) in equilibrium with chrome spinel using the regressions of Zaccarini et al., (2011), which are:

$$(Al_2O_{3melt}) = 5.2253\ln(Al_2O_{3spinel}) + 1.1232 \quad (1)$$

$$(TiO_{2melt}) = 1.0897(TiO_{2spinel}) + 0.0892 \quad (2)$$

As listed in Table 3, the melts parental to the spinels have Al_2O_{3melt} ranging from 9.48wt%–15.07wt%, and TiO_{2melt} ranging from 0.05wt%–0.92wt%, which is similar to that of the Troodos boninites (Cameron et al., 1985; Flower et al., 1987) and Thetford boninites (Page et al., 2008) respectively. This suggests that the North Hebei peridotites have been metasomatized by boninite-like melts.

In the classification diagram proposed by Kamenetsky et al., (2001) (Fig. 9), the spinel compositions of peridotite samples QLD02, DYG01, 05LHP02, 05LHP04 and LHPX02 plot in the "arc" and "SSZ peridotite" field, implying a genesis related to subduction. The compositions of samples LHPX01, LHPX02, 05LHP01 and 05LHP02 plot in the "MORB-SSZ peridotite" overlapping area, and spinel sample 05LHP01 plots in the "MORB peridotite" field, suggesting a genesis within the mantle beneath an ocean spreading center.

The silica-rich rocks (ZNP01 and ZNP02) have trace element patterns similar to Archean Whundo-type boninites (Smithies et al., 2004), suggesting a subduction-related origin. It is noted that the boninite-like samples have very high Yb/Sc (Fig. 7b) contrasting to the low Yb/Sc (Fig. 7a) of the peridotites. As Sc is preferentially hosted in mafic minerals (Doe, 1997), the compensative Yb-Sc distributions of the peridotites and the boninitic rocks (Fig. 7a–b) strongly suggest that the silica-rich rocks were originally mantle melts. Kelement et al., (1998) suggest that subduction-related melts would react with mantle peridotites to produce silica-rich peridotites. The coexistence of peridotites and boninite-like rocks in the

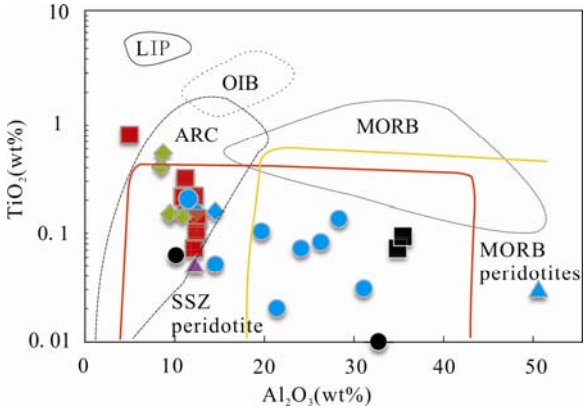


Fig. 9. Al_2O_3 vs TiO_2 compositional relationship in spinel (Kamenetsky et al., 2001).

study area indicates that the mantle peridotites have reacted with the boninite-like melts within a subduction-related setting. It is noteworthy that high-Cr spinels and high-Al spinels occur in a same peridotite sample 05LHP02. This may reflect the effect of late stage metasomatism of a peridotite that was located within a fluid-/magma-flow channel during the ascent of the subduction-related magma.

5.4 Ages of peridotites based on the Re-Os isotopes

Rhenium depleted model ages (T_{RD}) can provide the minimum constraints on the timing of mantle melt depletion events by assuming that a single melting event removes all of the Re from a peridotite and can therefore "freeze" the evolution of the isotopic composition of the mantle source along a chondritic path prior to that time (Walker et al., 1989; Shirey and Walker, 1998). As listed in Table 1, the peridotites from North Hebei Province have T_{RD} ages ranging from 748 Ma to 2055 Ma, indicating that the peridotites experienced melt depletion during the Precambrian. This age range is too large to represent the timing of one single melt depletion event for the studied peridotites, however these peridotites are unlikely to be the products of several different melt extraction events for the following reasons: Firstly, they have similar normative mineral compositions and similar chemical compositions; secondly, they are found together in a limited outcrop area; and thirdly, the peridotites from North Hebei Province both have >1wt% Al_2O_3 and as such are not highly refractory.

Multi-stage metasomatism, or metasomatism of variable intensity, may be a better explanation of the variable T_{RD} ages of the studied peridotites. Mantle-derived melt can transport several tens of ppt of Os (Shirey and Walker, 1998), and therefore repeated melt input during mantle metasomatism may introduce more radiogenic Os into the peridotites. This would result in the T_{RD} of the metasomatized peridotites to appear younger than the actual melt depletion event, and as a result the oldest T_{RD} (2055 Ma) may reflect the later limit of the melt depletion event.

Rhenium concentrations may be affected by later mantle metasomatism, so an "isochron age" cannot be obtained from the $^{187}Re/^{188}Os$–$^{187}Os/^{188}Os$ plot for the studied peridotites (not shown in this paper). Conveniently, Al is less easily perturbed during metasomatism since Al_2O_3 remains in the peridotite after nearly all of the Re has been removed during partial melting (Reisberg and Lorand, 1995). By using the extrapolation from Al_2O_{3PUM} to a value of 0.7% as suggested by Handler and Bennett (1999), we draw three "proxy isochrones" which intercept the $^{187}Os/^{188}Os$ axis at the values of 0.108, 0.111 and 0.117, corresponding to model ages of 2.7 Ga, 2.4 Ga and 1.4Ga respectively (Fig. 10). When plotted on an Al_2O_3-$^{187}Os/^{188}Os$ diagram, the most refractory (low Al) samples are close to the 2.4 Ga and 2.7 Ga "proxy isochrons". This suggests that melt extraction may occur around the end of the Neoarchean. The fertile samples have younger proxy model ages of around 1.4 Ga, however this may not represent the actual timing of the mantle melt depletion event because their Al abundance and Os isotopes may have been highly altered during subsequent metasomatic processes.

In summary, Re depleted model ages (T_{RD}) suggest that the peridotites experienced mantle melt depletion during the Precambrian; and Al proxy isochrons suggest minimum melt depletion ages of between 2.4 and 2.7 Ga. The apparently younger model ages of the more fertile peridotites may be the results of later metasomatism.

5.5 A lithospheric mantle and infiltrated melt suite formed in the North Hebei subduction zone

Petrological, geochemical, and mineral composition data suggest that the North Hebei peridotites were originally part of a residual mantle after melting at depth, implying that the peridotite belt from North Hebei Province was once part of the continental lithospheric mantle below the NCC. The peridotites differ from the cratonic mantle as represented by some high $Mg^{\#}$ mantle xenoliths (eg. Gao et al., 2002; Chu et al., 2009; Wu et al., 2006; Zhang et al., 2008), however they are similar to the supra-subduction zone peridotite suite in the central orogenic belt of the NCC (Polat et al., 2005). A subduction-related origin is also supported by the coexistence of the boninite-like rocks and the peridotites, with the former having geochemical compositions similar to Archean Whundo-type boninites (Smithies et al., 2004). The peridotites from North Hebei Province do not seem to be a part of the accreted supra-subduction mantle of the central orogen, as they occurr along the E-W striking

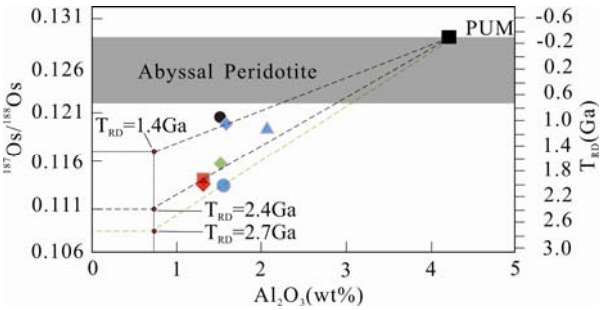


Fig. 10. Os isotopic composition versus Al_2O_3 (wt%) for all samples.

The abyssal peridotite data are from Reisberg et al. (1995) and Brandon et al. (2000). Primitive Upper Mantle (PUM) value is from Meisel et al. (2001).

major fault and coexist with metamorphic lithologies from the Inner Mongolia–North Hebei Orogen near the northern margin of the NCC (Fig. 1a) (Kusky et al., 2007; Zhai and Santosh, 2011). In light of this, we suggest that the peridotites and boninite-like rocks distributed in the North Hebei Province represent part of the lithospheric mantle that was accreted to the NCC during Paleoproterozoic subduction along the North Hebei Orogen.

6 Conclusions

(1) The peridotites from North Hebei Province were originally harzburgites that experienced a high degree of melt extraction and subsequent mantle metasomatism in a subduction zone setting.

(2) Silica-rich samples coexisting with peridotites have protolithic compositions similar to Archean boninites.

(3) Re-Os isotopes of the peridotites yield melt extraction ages between the Late-Achaean to Early Paleoproterozoic.

(4) The peridotite-boninite suite from North Hebei Province may represent accreted continental lithospheric mantle after subduction-related melt extraction and metasomatic processes in the North Hebei Orogeny at the northern margin of the NCC.

Acknowledgements

This study was financially supported by the NSFC(grant no. 41430207, 41602340) and China Postdoctoral Science Foundation （2016M591246). Guiming Shu is thanked for assistance on EPMA analysis.

Manuscript received Mar. 28, 2016
accepted Dec. 26, 2016
edited by Fei Hongcai

References

Allen, D.E., and Seyfried, W.E., 2005. REE controls in ultramafic hosted MORB hydrothermal systems: an experimental study at elevated temperature and pressure. *Geochimi. Cosmochim. Acta*., 69 (3): 675–683.

Asimow, P.D., and Langmuir, C.H., 2003. The importance of water to ocean ridge melting regimes. *Nature*, 421: 815–20.

Barnes, S.J., and Roeder, P.L., 2001. The range of spinel compositions in terrestrial mafic and ultramafic rocks. *J. Petrol*., 12: 2279–2302.

Ballhaus, C., Berry R.F., and Green, D.H., 1991. High pressure experimental calibration of the olivine-orthopyroxene-spinel oxygen geobarometer: implications for the oxidation state of the upper mantle. *Contrib. Mineral. Petrol.*, 107: 27–40.

Baumgartner, R.J., Zaccarini, F., Garut, G., and Thalhammer, O.R.A., 2013. Mineralogical and geochemical investigation of layered chromitites from the Bracco–Gabbro complex, Ligurian ophiolite, Italy. *Contrib. Mineral. Petrol.*, 165: 477–493.

Bodinier, J.-L., Vasseur, G., Vernières, J., Dupuy, C., and Fabriès, J., 1990. Mechanisms of mantle metasomatism: geochemicalevidence from the Lherz orogenic peridotite. *Journal of Petrology*, 31:597–628.

Brandon, A.D., Snow, J.E., Walker, R.J., Morgan, J.W., and Mock, T.D., 2000. ^{190}Pt–^{186}Os and ^{187}Re–^{187}Os systematics of abyssal peridotites. *Earth Planet. Sci. Lett.*, 177: 319–335.

Bruce, R.D., 1997. Geochemistry of oceanic igneous rocks-ridges, islands, and arcs-with emphasis on manganese, scandium, and vanadium. *Inter. Geo. Revi.*, 39(12): 1053–1112.

Cameron, W.E., 1985. Petrology and origin of primitive lavas from the Troodos ophiolite, Cyprus. *Contrib. Mineral. Petrol.*, 89: 239–255.

Chen Anguo, Wang Jizhong and Peng Lan, 1996. Geological characteristics of ultrabasic rocks in North Hebei Province. *Jour. Hebei. Colle. Geol.*, 19: 3–4 (In Chinese).

Chen, M.M., Tian, W., Suzuki, K., Tejada, M.L.G., Liu, F.L., Ryoko, S., Wei, C.J., Chen, B., and Chu, Z.Y., 2014. Peridotite and pyroxenite xenoliths from Tarim, NWChina: Evidences for melt depletion and mantle refertilization in the mantle source region of the Tarim flood basalt. *Lithos*, 204: 97–111.

Chu, Z.Y., Wu, F.Y., Walker, R.J., Rudnick, R.L., Pitcher, L., Puchtel, I.S., Yang, Y.H., and Wilde, S.A., 2009. Temporal evolution of the lithospheric mantle beneath the eastern North China Craton. *J. Petrol.*, 50(10): 1857–1898.

Deer, W.A., Howie, R.A., and Zussman, J., 1992. An introduction to the rock-forming minerals. Harlow, England (ed.), *Longman Sci. and Techno.*, pp., 695.

Deschamps, F., Godard, M., Guillot, S., and Hattori, K., 2013. Geochemistry of subduction zone serpentinites: a review. *Lithos.*, 178: 96–127.

Ionov, D.A., Bodinier, J., Mukasa, SB., and Zanetti, A, 2002. Mechanisms and sources of mantle metasomatism: major and trace element compositions of peridotite xenoliths from Spitsbergen in the context of numerical modeling. *J. Petrol.*, 43(12): 2219–2259.

Flower, M.F.J., and Levine, H.M., 1987. Petrogenesis of a tholeiite-boninite sequence from Ayios Mamas, Troodos ophiolite: evidence for splitting of a volcanic arc? *Contrib. Mineral. Petrol.*, 97: 509–524.

Frey, F.A., and Prinz, M., 1978. Ultramafic inclusions from San Carlos, Arizona: Petrologic and geochemical data bearing on their pedogenesis. *Earth. Planet. Sci. Lett.*, 38: 129–176.

Gao, S., Roberta, L.R., Richard, W.C., William, F.M., and Liu, Y.S., 2002. Re-Os evidence for replacement of ancient mantle lithosphere beneath the North China craton. *Earth Planetary. Sci. Lett.*, 198: 307–322.

Green, E., Hooland, T., and Powell, R., 2007. An order–disorder model for omphacitic pyroxenes in the system jadeite-dispside -hedenbergite-acmite, with application to eclogitic rocks, *Ameri. Mineral.*, 92(7): 1181–1189.

Guo, J.H., Zhai, M.G., and Xu, R.H., 2001. Timing of the granulite-facies metamorphism in the Sanggan area, North China craton: zircon U-Pb geochronology. *Sci. in China (Series D)*, 44(11): 1010–1018.

Guo, J.H., Chen, Y., Peng, P., Liu, F., Chen, L., and Zhang, L.Q., 2006. Sapphirine-bearing granulite in Daqingshan, Inner Mongolia: 1.8Ga UHT metamorphic event. In: *Abstract*

Volume of Petrology and Earth dynamics in China. Nanjing: Nanjing University: 215–218.

Handler, M.R., and Bennett, V.C., 1999. Behaviour of platinum-group elements in the subcontinental mantle of eastern Australia during variable metasomatism and melt depletion. *Geochim. Cosmochim. Acta*, 63: 3597–3618.

Hao, X.L., and Li, Y.L., 2013. ^{57}Fe Mössbauer spectroscopy of mineral assemblages in mantle spinel lherzolites from Cenozoic alkali basalt, eastern China: Petrological applications. *Lithos*, 156–159: 112–119.

Herzberg, C., and O'Hara, M.J., 2002. Plume-associated ultramafic magmas of Phanerozoic age. *J. Petrol.*, 43: 1857–1883.

Herzberg, C., 2004. Geodynamic information in peridotite petrology. *J. Petrol.*, 45(12): 2507–2530.

Himmelberg, G.R., and Loney, R.A., 1973. Petrology of the Vulcan Peak Alpine-type peridotite, southwestern Oregon. *Geol. Soci. of Ameri Bull.*, 8: 1585–1600.

Hu L., Song, H., Yan, D. and Hu, D.G., 2003. The 40Ar/39Ar geochronology constraint and geological significance of mylonites in Shangyi-Chicheng fault belt on the north of North China Craton. *Sci. China. Earth. Sci.*, 46(1): 1134–1141.

Jahn, B.M., Fan, Q.C., Yang, J.J., and Henin, O., 2003. Petrogenesis of the Maowu pyroxenite-eclogite body from the UHP metamorphic terrane of Dabieshan: chemical and isotopic constrains. *Lithos*, 70: 243–267.

Johnson, K.T.M., Dick, H.J.B., and Shimizu N., 1990. Melting in the oceanic upper mantle: An ion microprobe study of diopsides in abyssal peridotites. *J. Geophysi. Res.*, 95(B3): 2661–2678.

Kamenetsky, V.S., Crawford, A.J., and Meffre, S., 2001. Factors controlling chemistry of magmatic spinel: an empirical study of associated olivine, Cr-spinel and melt inclusions from primitive rocks. *J. Petrol.*, 42: 655–671.

Katz, R.F., Spiegelman, M., and Langmuir, C.H., 2003. A new parameterization of hydrous mantle melting, *Geochem. Geophys. Geosyst*., 4(9): 1073.

Kelemen, P.B., Dick, H.J.B., and Quick, J.E., 1992. Formation of harzburgite by pervasive melt/rock reaction in the upper mantle. *Nature* 358, 635–641.

Kelemen, P.B., and Stanley, R.H., and Stefan, B., 1998. Silica enrichment in the continental upper mantle via melt/rock reaction. *Earth Planet Sci. Lett.*, 164: 387–406.

Kerrich, R., Wyman, D., Fan, J., and Bleeker, W., 1998. Boninite series: low-Ti tholeiite associations from the 2.7 Ga Abitibi greenstone belt. *Earth Planet. Sci. Lett.*, 164: 303–316.

Kimura J.I. and Nakajima J., 2014. Behaviour of subducted water and its role in magma genesis in the NE Japan arc: A combined geophysical and geochemical approach. *Geochi et Cosmochi Acta*, 143: 165–188.

Kusky, T.M., Windley, B.F., and Zhai, M.G., 2007. Tectonic evolution of the North China Block: From orogen to craton to orogen. In: Zhai, M.G., Windley, B.F., and Kusky, T. (eds.), *Mesozoic sub-continental thinning beneath eastern North China.* Geol. Soci., London, Special Publications, 280: 1–34.

Kusky, T.M., Li, J.H., Raharimahefa, T., and Carlson, R.W., 2004b. Re–Os isotope chemistry and geochronology of chromite from mantle podiform chromites from the Zunhua ophiolitic mélange belt, N. China: correlation with the Dongwanzi ophiolite, Chapter 8. In: Kusky, T.M. (ed.), *Precambrian Ophiolites and Related Rocks*. Devel. Precambrian Geol., 13: 275–282.

Langmuir, C.H., Klein, E.M., and Plank, T., 1992. Petrological systematics of mid-ocean ridge basalts: constraints on melt generation beneath ocean ridges. In: Phipps, M.J., Blackman, D.K., and Sinton, J.M. (eds.), *Mantle Flow and Melt Generation at Mid-ocean Ridges*. Ameri Geophysi. Uni. Monograph., 71: 183–280.

Li, J.P., and Wang, J., 2002. Mantle redox state evolution in eastern China and its implications. *Acta Geologica Sinica* (English Edition), 76(2): 238–248.

Liu, S.W., Lü Y.J., Feng, Y.G., Liu X.M., Yan, Q.R., Zhang, C., and Tian, W., 2007. Zircon and monazite geochronology of the Hongqiyingzi complex, northern Hebei, China. *Geol. Bull. Chin*., 26(9): 1086–1100 (In Chinese).

Liu, J.F., Li, J.Y., Qu, J.F., Hu, Z.C., Guo, C.L., and Chen, J.Q., 2016. Petrogenesis of Lanqizhen Paleoproterozoic garnet granite at Longhua area in the northern margin of the North China craton and its geological significance. *Acta Geologica Sinica*, 90: 2365–2383 (In Chinese with English abstract)

Meisel, T., Walker, R.J., Irving, A.J., and Lorand, J.P., 2001. Osmium isotopic compositions of mantle xenoliths: a global perspective. *Geochim. Cosmochim. Acta.*, 65: 1311–1323.

Menzies, M., Long, A., Ingram, G., Tatnell, M., Janecky, D.R., 1993. MORB peridotite–seawater interaction: experimental constraints on the behaviour of trace elements, ^{87}Sr/^{86}Sr and ^{143}Nd/^{144}Nd ratios. In: Prichard, H.M., Alabaster, T., Harris, N.B.W., Neary, C.R. (eds.), *Magmatic processes and plate tectonics*. Geological Society Special Publications, 76, 309–322.

Morten, L., Taylor, L.A., and Durazzo, A., 1989. Spinels in harzburgite and lherzolite inclusions from the San Giovanni Ilarione Quarry, Lessini Mountains, Veneto region, Italy. *Mineral. Petrol.*, 40: 73–89.

Négrel, P., Guerrot, C., Cocherie, A., Azaroual, M., Brach, M., and Fouillac, C., 2000. Rare earth elements, neodymium and strontium isotopic systematics in mineral waters: evidence from the Massif Central, France. *Applied Geochemistry*, 15: 1345–1367.

Ni, Z.Y., Zhai, M.G., Wang, R.M., Tong, Y., Shu, G.M., and Hai, X.L., 2004. Discovery of Late Paleozoic retrograded ecologites from the middle part of the northern margin of North China Craton. *Chinese Sci. Bull.*, 49(6): 600–606.

Ni, Z.Y., Zhai, M.G., Wang, R.M., and Tong, Y., 2006. Late Paleozoic retrograded eclogites from within the northern margin of the North China Craton: Evidence for subduction of the Paleo-Asian ocean. *Gondwana Res.*, 9: 209–224.

Niu, Y., 2004. Bulk-rock major and trace element compositions of abyssal peridotites: implications for mantle melting, melt extraction and post-melting processes beneath mid-ocean ridges. *Journal Petrol*., 45(12): 2423–458.

Niu, Y., and Batiza, R., 1991. An empirical method for calculating melt compositions produced beneath mid-ocean ridges: application for axis and off-axis (seamounts) melting. *J. Geophysi. Res.*, 96: 21753–21777.

O'Neill, H.St.C., and Wall, V.J., 1987. The olivine-orthopyroxene-spinel oxygen geobarometer, the nickel precipitation curve, and the oxygen fugacity of the Earth's upper mantle. *J. Petrol.*, 28: 1169–1191.

Pagé, P., Bédard, J.H., Schroetter, J.M., and Tremblay, A., 2008. Mantle petrology and mineralogy of the Thetford Mines

Ophiolite Complex. *Lithos*, 100: 255–292.

Paulick, H., Bach, W., Godard, M., De Hoog, J.C.M., Suhr, G., and Harvey, J., 2006. Geochemistry of abyssal peridotites (Mid-Atlantic Ridge, 15°20'N, ODP Leg 209): Implications for fluid/rock interaction in slow spreading environments. *Chemical Geology*, (234): 179–210.

Peng, P., Guo, J.H., Zhai, M.G., and Bleeker, W., 2010. Paleoproterozoic gabbronoritic and granitic magmatism in the northern margin of the North China craton: Evidence of crust–mantle interaction. *Precambrian Res.*, 183: 635–659.

Peng, P., Li, Y., Liu, F., Wang, F., 2012. Geological relation of Late Archean lithologic units in Northwest Heber, North China Craton: Implication for building of early continental crust. *Acta Petrol. Sinica*, 28(11): 3531–3544 (in Chinese with English abstract).

Polat, A., Kusky, T., and Li, J.H., 2005. Geochemistry of Neoarchean (ca. 2.55–2.50 Ga) volcanic and ophiolitic rocks in the Wutaishan greenstone belt, central orogenic belt, North China craton: Implications for deodynamic setting and continental growth. *Bull. Geol. Soci. Ameri.*, 117: 1387–1399.

Powell, R., and Holland, T., 1999. Relating formulations of the thermodynamics of mineral solid solutions: Activity modeling of pyroxenes, amphiboles, and micas. *Ameri. Mineral.*, 84(1–2): 1–14.

Powell, R., and Holland, T., 1998. An internally consistent thermodynamic data set for phases of petrological interest. *J. Metamorphic Geol.*, 16: 309–343.

Reisberg, L.C., and Lorand, J.P., 1995. Longevity of sub-continental mantle lithosphere from Osmium isotope systematics in orogenic peridotite massifs. *Nature*, 376: 159–162.

Salters, V.J.M., and Stracke, A., 2004. Composition of the depleted mantle. *Geochemistry, Geophysics, Geosystems*, 5 (5): 469–484.

Santosh, M., Zhao, D.P., and Kusky, T.M., 2010. Mantle dynamics of the Paleoproterozoic North China Craton: a perspective based on seismic tomography. *J. Geody.*, 49: 39–53.

Sarafian, E., Gaetani, G.A., Hauri, E.H., and Sarafian A.R., 2017. Experimental constraints on the damp peridotite solidus and oceanic mantle potential temperature. *Science*, 355, 942–945.

Shirey, S.B., and Walker, R.J., 1998. The Re–Os isotope system in cosmochemistry and high temperature geochemistry. *Ann. Rev. Earth Planet. Sci.*, 26: 423–500.

Smithies, R.H., Champion D.C., and Sun, S.S., 2004. The case for Archaean boninites. *Contri. Mineral. Petrol.*, 147: 705–721.

Smoliar, M.I., Walker, R.J., and Morgan, J.W., 1996. Re–Os ages of group IIA, IIIA, IVA, and IVB meteorites. *Science*, 271:1099–1102

Snow, J.E., and Reisberg, L., 1995. Os isotopic systematics of the MORB mantle: results from altered abyssal peridotites. *Earth Planet. Sci. Lett.*, 136: 723–733.

Staudigel, H., and Hart, S.R., 1983. Alteration of basaltic glass: Mechanisms and significance for the oceanic crust-seawater budget. *Geochim. Et. Cosmochim. Acta.*, 47: 337–350.

Sun, S.S., and McDonough, W.E., 1989. Chemical and isotopic systematics of oceanic basalts: implications for mantle composition and processes. In: Saunders, A.D., and Norry, M.J., (eds.), *Magmatism in the Ocean Basins*. Geol. Soci., London, Special Publications, 42: 313–345.

Tang, Y.J., Zhang, H.F., Ying, J.F., and Su, B.X., 2013. Widespread refertilization of cratonic and circum-cratonic lithospheric mantle. *Earth. Sci. Revi.*, 118: 45–68.

Tian, W., Chen, B., Liu, C.Q. and Zhang, H.F., 2007. Zircon U-Pb age and Hf isotopic compostion of the Xiaozhangjiakou ultramafic pluton in northern Hebei. *Acta Petrol. Sinica*, 23 (3): 583–590 (in Chinese with English abstracts).

Walker, R.J., Carlson, R.W., Shirey, S.B., and Boyd, F.R., 1989. Os, Sr, Nd and Pb isotope systematics of southern African peridotite xenoliths: implications for the chemical evolution of subcontinental mantle. *Geochim. Cosmochim. Acta*, 53: 1583–1595.

Walter, M.J., 1998. Melting of garnet peridotite and the origin of komatiite and depleted lithosphere. *Journal Petrol.*, 39: 29–60.

Walter, M.J., 2003. Melt extraction and compositional variability in mantle lithosphere. *Treatise on Geochemistry*, 2: 363–394.

Wan, Y.S., Liu, D.Y., Dong, C.Y., Xu, Z., Wang, Z., Wilde, S., Yang, Y.X., Liu, Z.P., and Zhou, H., 2009. The Precambrian khondalite belt in the Daqingshan Area, North China craton: Evidence for multiple metamorphic events in the Paleoproterozoic era. *Geol. Soci. Speci. Publi. Lon.*, 323: 73–97.

Wang, Y.S., Liu, S.J., Kroner, A., Dong, C.Y., Xie, H.Q., Xie, S.W., Bai, W.Q., Ren, P., Ma, M.Z., and Liu, D.Y., 2016. Eastern ancient terrane of the North China Craton. *Acta Geologica Sinica* (English Edition), 90(4): 1082–1096.

White, R.W., Powell, R., and Holland, T., 2007. Progress relating to calculation of partial melting equilibria for metapelites. *J. Metamorphic Geol.*, 25(5): 511–527.

Wu, F.Y., Walker, R.J., Yang, Y.H., Yuan, H.L., and Yang, J.H., 2006. The chemical-temporal evolution of lithospheric mantle underlying the North China Craton. *Geochim. Cosmochim. Acta.*, 70: 5013–5034.

Zaccarini, F., Garuti, G., Proenza, J.A., Campos, L., Thalhammer, O.A.R., Aiglsperger, and Lewis, J., 2011. Chromite and platinum-group-elements mineralization in the Santa Elena ophiolitic ultramafic nappe (Costa Rica): geodynamic implications. *Geol. Acta.*, 9: 407–423.

Zhai, M.G., 2011. Cratonization and the Ancient North China Continent: A summary and review. *Sci. China. Earth. Sci.*, 54: 1110–1120. doi: 10.1007/s11430-011-4250-x.

Zhai, M.G., Guo, J.H., Yan, Y.H., Li, Y.G., and Han, X.L., 1992. The discovery of high-pressure basic granulite in the Archean north China craton and preliminary study. *Sci. China. (Series B)*, 12: 1325–1300.

Zhai, M.G., Guo, J.H., Li, J.H., Yan, Y.H., Li, Y.G., and Zhang, W.H., 1995. The discoveries of retrograde eclogites in North China craton in Archaean. *Chinese Sci. Bull.*, 40: 1590–1594.

Zhai, M.G., and Santosh, M., 2011. The early Precambrian odyssey of the North China Craton: A synoptic overview. *Gondwana. Res.*, 20: 6–25.

Zhang, H.F., Steven, L.G., Zhou, X.H., Sun, M., Zheng, J.P., and Cai, Y., 2008. Evolution of subcontinental lithospheric mantle beneath eastern China: Re–Os isotopic evidence from mantle xenoliths in Paleozoic kimberlites and Mesozoic basalts. *Contrib. Mineral. Petrol.*, 155: 271–293.

Zhao, G.C., Sun, M., Wilde, S.A., and Li, S.Z., 2005. Late Archean to Paleoproterozoic evolution of the North China Craton: key issues revisited. *Precambrian Res.*, 136: 177–202.

Zhao, G.C., Cawood, P.A., Wilde, S.A., Sun, M., and Lu, L.Z., 2000a. Metamorphism of basement rocks in the central zone of the North China Craton: implication for Paleoproterozoic tectonic evolution. *Precambrian Res.*, 103: 55–88.

Zhao, L., Zhu, X.Y., and Zhai, M.G., 2016. Major advances in the study of the Precambrian geology and metallogenesis of the North China Craton: A review. *Acta Geologica Sinica* (English Edition), 90(4): 1122–1155.

Zheng, J.P., O'Reilly, S.Y., and Griffin, W.L., 1999. Mantle xenoliths from kimberlites, Shandong and Liaoning: Paleozoic mantle character and its heterogeneity. *Acta Petrol. Sinica*, 15 (1): 65–75 (in Chinese with English abstract).

Zhou, M.F., Paul, T.R., Su, B.X., Gao, J.F., Li, J.W., Yang, J.S., and Malpas, J., 2014. Compositions of chromite, associated minerals, and parental magmas of podiform chromite deposits: The role of slab contamination of asthenospheric melts in suprasubduction zone environments. *Gondwana Res.*, 26: 262–283.

About the first author:

TIAN Wei: received a B.S. (1998) in geology and a Ph.D. (2003) in igneous petrology from Peking University. Since 2003 he has worked as an assistant professor in petrology at the School of Earth and Space Sciences, Peking University. In 2007, he became an associate professor in igneous petrology and volcanology.